Article

INTERNATIONAL JOURNAL OF DAMAGE MECHANICS

International Journal of Damage Mechanics
22(5) 683–698

DOI: 10.1177/1056789512462428
ijd.sagepub.com

SAGE

Modeling creep damage of an aluminum–silicon eutectic alloy

Holm Altenbach[1], Sergii Kozhar[2] and Konstantin Naumenko[1]

Abstract

Aluminum–silicon casting alloys are widely used in the automotive industry. The aim of this article is to analyze creep and creep damage of the eutectic AlSi12CuNiMg cast piston alloy and to present a constitutive model that reflect basic features of deformation, aging and damage behavior. Creep tests and force-controlled low cycle fatigue tests are carried out at several levels of temperature. Creep curves exhibit classical three stages. The tertiary creep stage is controlled by damage processes, mainly due to failure of the brittle inclusions and aging processes of the aluminum matrix. Ruptured specimens are analyzed with the help of optical and scanning electron microscopy to establish the fracture mode. A constitutive model is developed to describe the high temperature creep and ratcheting behavior. The proposed model involves three state variables including a back stress, an aging parameter and a damage variable. The model is calibrated against the creep and tensile curves and verified by numerical simulations of cyclic creep tests.

Keywords

Creep, low cycle fatigue, ratcheting, aluminum-silicon alloy, constitutive model

Introduction

Cast aluminum–silicon (Al–Si) base alloys belong to the most important aluminum alloys attributed to their low density, high specific strength, good castability and wear resistance.

The eutectic aluminum alloy AlSi12CuNiMg investigated in the present work is widely used for load-bearing structural components in the automotive industry. Its most important areas of application are pistons for combustion engines, gears, pump parts, wear-resistant and heat-resistant parts of all kinds owing to its high strength at elevated temperatures and low thermal expansion coefficient. Structural components, for example pistons, may be subjected to complex thermo-mechanical

[1]Otto-von-Guericke-University Magdeburg, Institute of Mechanics, Magdeburg, Germany
[2]Institute of Solids Process Engineering and Particle Technology, Hamburg University of Technology, Hamburg, Germany

Corresponding author:
Holm Altenbach, Otto-von-Guericke-University Magdeburg, Institute of Mechanics, D-39106 Magdeburg, Germany.
Email: holm.altenbach@ovgu.de

loading paths. Therefore it is important to analyze this alloy under applied cyclic loading conditions at high temperature (Moreira and Fuoco, 2006; Silva, 2006).

Numerous studies of Al–Si alloys show that the static strength and fatigue behavior strongly depend on casting defects and microstructural characteristics. The presence of casting porosity and oxide films decreases the fatigue life (Ammar et al., 2008a, 2008b; Couper et al., 1990; Stroppe, 2000). On the other hand, in the absence of casting imperfections, the fatigue fracture of cast Al–Si alloys is mainly characterized by cracking and debonding of silicon and intermetallic particles and nucleation of voids in the aluminum matrix. Dendrite arm spacing, grain size, shape and distribution of silicon particles and intermetallic compounds can also significantly influence the behavior of cast Al–Si alloys (Ye, 2002).

In this study, the alloy behavior with respect to tensile strength, creep as well as isothermal mechanical fatigue at different temperatures is examined. To describe the results of conducted tests, a constitutive model is developed. The model is calibrated against the creep and tensile curves and verified by numerical simulations of cyclic creep tests.

Experimental procedure

The material used in this study is cast aluminum alloy EN AC-48000. The chemical composition of the alloy is given in Table 1. The base alloy was supplied in the form of ingots which were cut and melted in a preheated silicon carbide crucible of 3 kg capacity, using an electrical resistance furnace and keeping the melting temperature at 740°C. Phosphorous was added with the help of the AlCu19P1,4 master alloy. Subsequently, the melts were degassed with the tablet degassing method. The melt was then poured into a permanent steel mold (Figure 1) and preheated to 250°C. Samples were heat-treated under T6 conditions, i.e. solution treated at 510°C for 6 h in an air circulate furnace, water quenched, naturally aged at room temperature for 24 h, and then

Table 1. Chemical composition of the studied alloy (wt%).

Si	Cu	Ni	Mg	Mn	Fe	Ti	P	Sr	Al
12.72	1.07	0.95	1.12	0.16	0.41	0.05	0.005	<0.0005	Balance

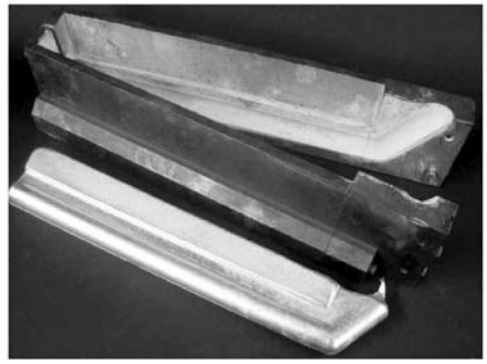

Figure 1. Casting mold according to DIN 29531.

artificially aged at 165°C for 8 h. Microstructural changes were examined using optical and scanning electron microscopy (SEM).

Tensile testing of specimens was carried out at room temperature and up to 300°C in a Zwick Z250 machine in accordance with the DIN EN 10002 procedure. The strain rate sensitivity of simple mechanical properties are determined with the help of additional tensile test at 300°C. The hardness of the as-cast and heat-treated specimens was measured in a Brinell hardness tester with a load of 62.5 kg and a ball diameter of 2.5 mm.

Specimens for creep and fatigue testing with a diameter of 5 mm, length of 120 mm and gage length of 50 mm were machined from the ingots. The surfaces of the specimens were polished to avoid crack initiation from the surface due to machining imperfections. Tests were performed on a servohydraulic testing machine MTS-810 with maximum load of 250 kN. To measure the strain, an extensometer with a gage length of 12.5 mm was applied. The specimens were heated with a 5 kW induction heater. The thermal strain was subtracted from the total strain. In all experiments the test specimens were held during 15 min at the proof temperature before mechanical testing.

Creep tests were carried out at temperatures of 250°C and 300°C. Force-controlled fatigue tests were conducted in the temperature range of 20–300°C in laboratory air with test frequencies of 0.1 and 1 Hz under low cycle fatigue conditions, which means that fatigue lives are less then 10^5 cycles to failure according to DIN EN 3874. The specimens were subjected to triangular stress cycle with $R_\sigma = 0$, where R_σ is the stress ratio. Therefore the applied cyclic loading corresponds to the pure tensile regime without stress reversals. Some of the broken specimens were analyzed with the help of light microscopy and SEM to determine the damage mechanisms.

Experimental results and discussion

The microstructure of the investigated alloy is presented in Figure 2. The aluminum matrix of the alloy contains primary coarse silicon as well as eutectic acicular silicon and numerous intermetallics. Addition of phosphorus has led to the refinement of the primary silicon crystals in the alloy. The effect of T6 heat treatment results in changes in the morphology, i.e. both the primary silicon crystals and eutectic silicon fibers are spheroidized and the strengthening compounds are well dispersed in the aluminum matrix.

The Brinell hardness for the alloy in as-cast condition at 20°C is determined as HB 87. After T6-heat-treatment the hardness has reached the value of HB 144. The achieved values of basic mechanical properties coincide with the literature data (Klatt et al., 1993) and hence are not

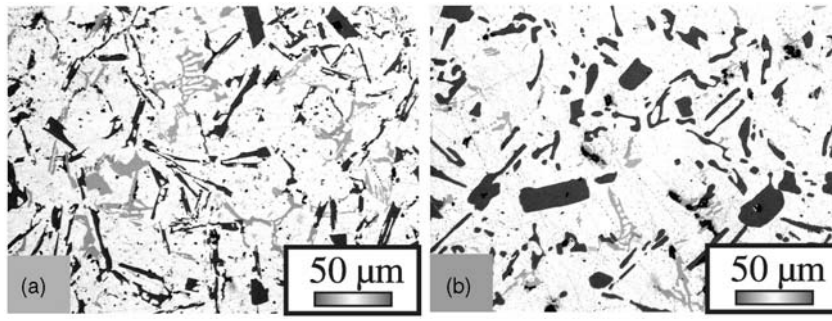

Figure 2. Light microscope observation of alloy microstructure in: (a) as-cast and (b) in heat-treated state.

listed here. The dependence of tensile properties on applied strain rate at 300°C is given in Table 2. Figure 3 shows the creep strain versus time curves. Owing to the scatter of test results, creep curves are averaged. Figure 4(a) shows the creep strength (stress versus time to rupture) curves for the temperature levels of 250°C and 300°C. The experimental data at 350°C published in Eswara-Prasad et al. (2000) is added to the plot. In the double logarithmic scale the data can be fitted by straight lines. The slopes of the lines depend on temperature levels. This fact indicates that different fracture mechanism may operate depending on stress and temperature values. The rupture strain versus stress plot is presented in Figure 4(b). We observe that values of rupture strain tend to decrease with an increase in the stress.

Table 2. Average tensile mechanical properties at 300°C in relation to the strain rate.

	Strain rate (1/s)			
	1×10^{-4}	8×10^{-4}	3.3×10^{-3}	3×10^{-2}
0.2% proof stress (MPa)	93	125.5	130	138.5
Tensile strength (MPa)	116	134.1	138.6	149
Ultimate elongation (%)	1.295	0.95	1.2	1.965

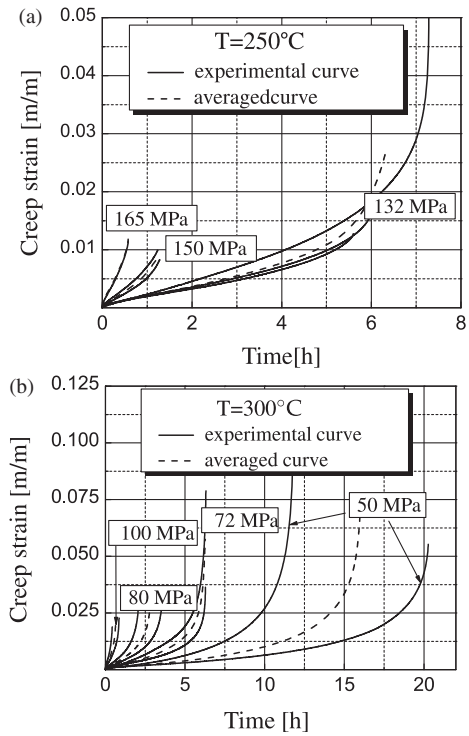

Figure 3. Experimental and averaged creep curves at: (a) 250°C and (b) 300°C.

The results of force-controlled low cycle fatigue tests for all temperatures are shown in Figure 5. The averages of fatigue lives obtained after several fatigue tests for each maximum stress value are straight lines in a semi-logarithmic plot. The increase in the total strain, i.e. strain ratcheting, is found for all specimens during the cyclic loading tested at temperatures above 250°C. The values of the maximum stress in a cycle as a function of time to rupture are compared in Figure 6.

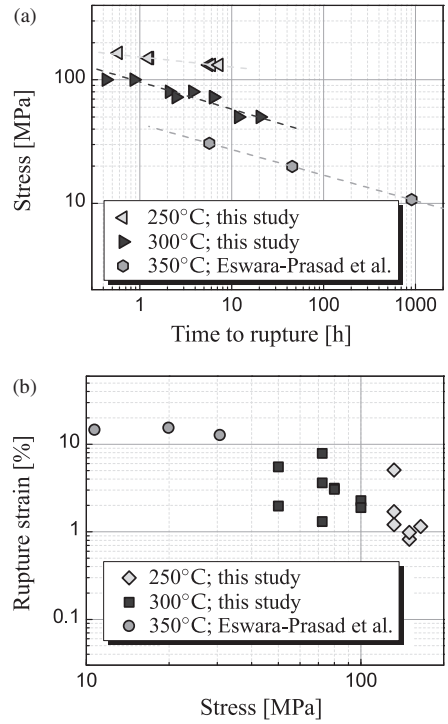

Figure 4. Variation of rupture time with stress (a) and the rupture strain vs stress (b).

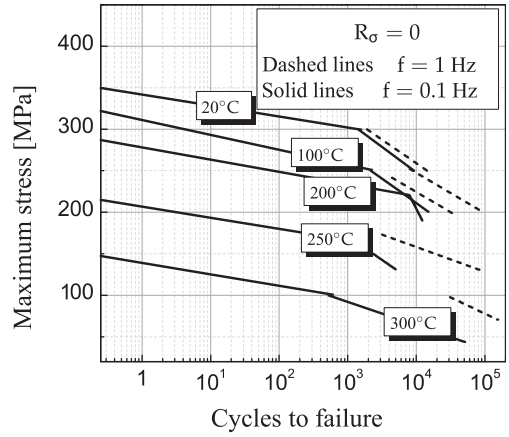

Figure 5. Relationship between applied maximum stress and fatigue life for investigated alloy.

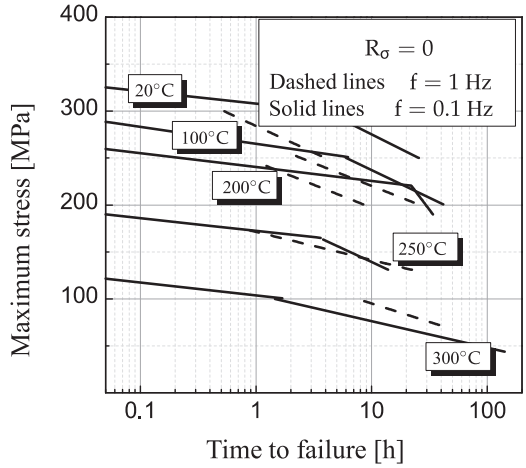

Figure 6. Relationship between applied maximum stress and time to failure for investigated alloy.

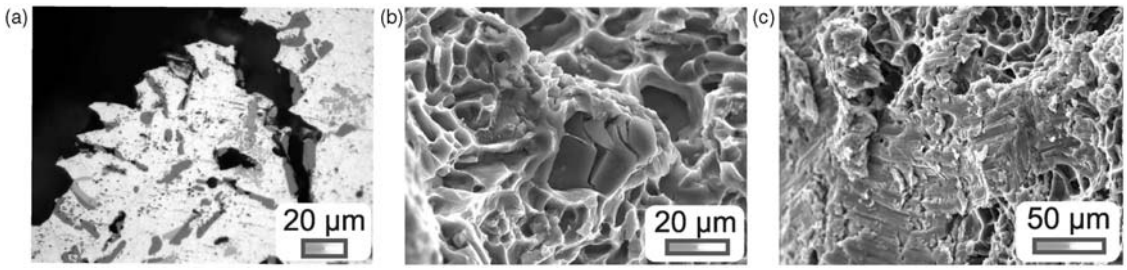

Figure 7. Optical micrograph of longitudinal sections of a broken fatigue specimen (a); SEM images of specimens fatigued at 300°C: cracked primary silicon (b) and fatigue striations (c).
SEM: scanning electron microscopy.

Specimens tested at temperatures of 20°C, 100°C as well as 200°C show a pure brittle fatigue fracture mode since the inelastic strain during loading is negligible. Starting up with a temperature of 250°C, the inelastic strain accumulates with the increasing number of cycles. The measured strain at rupture reaches the maximum values of 3.5% at 250°C and 10% at 300°C, respectively. It is observed in all LCF tests that a higher loading frequency results in an increase of the number of cycles to specimen failure. Comparing the life times at two loading frequencies we conclude that the higher loading frequency decreases time to rupture at temperatures up to 200°C, almost does not affect the rupture time at 250°C and increases the time to rupture at temperature of 300°C. To establish the fracture mode, several ruptured specimens are analyzed with the help of optical and SEM. Primary silicon particles in the alloy have a detrimental influence on fatigue behavior at all proof temperatures. Cracking was often observed, particularly in large particles with a higher aspect ratio. Silicon particles as well as brittle intermetallics appear to be sites for crack nucleation and propagation during loading (Figure 7(a)). The decohesion and cracking of silicon particles at the fracture surface (Figure 7(b)) reveal that these particles contribute to increasing the propagation rate

of fatigue cracks and to shortening the fatigue life. The fracture process also includes the coalescence of voids and dimples in the matrix around those broken hard particles. A few zones with fatigue striations have been found on the fracture surfaces (Figure 7(c)); such fracture morphology is more typical for structures which are subjected to high cycle fatigue loading. For all specimens tested at 250°C and at 300°C, the fracture morphology consists of cleavage fracture of brittle-phase precipitates and cellular ductile fracture of the aluminum matrix with a high density of microdimples. In order to describe the experimental results, the theoretical model must take into account visco-plastic material response, aging processes in a matrix and breakage of hard phases.

In order to describe the experimental results, the theoretical model must take into account visco-plastic material response, aging processes in a matrix and breakage of hard phases.

Constitutive model

As experimental data show, at high temperatures the tensile behavior is strain rate dependent. A unified theory of viscoplasticity has been developed to describe inelastic responses of engineering materials under different loading conditions, Abdel Karim and Ohno (2000); Colak and Krempl (2003); Inoue et al. (1989); Kang et al. (2006); Kowalewski et al. (1994); Krempl and Choi (1992); Ohno and Wang (1995); Yang (2007); Yang et al. (2003); Zhan and Tong (2007), among others. The constitutive equations characterize basic features of inelastic material behavior such as uni- and multi-axial ratcheting, creep, thermo-mechanical fatigue, etc. Any viscoplastic constitutive equation must include the viscosity function and the internal state variables together with appropriate evolution equations (Chaboche, 2008).

Several equations are available to describe the variation of minimum strain rate with applied stress during steady-state creep regime, e.g. Naumenko and Altenbach (2007)

- Norton (1929); Bailey (1929)

$$\dot{\varepsilon}_{\mathrm{eq}}^{\mathrm{cr}} = a\sigma_{\mathrm{eq}}^{\mathrm{n}} \tag{1}$$

- Prandtl (1928); Nadai (1938); McVetty (1943)

$$\dot{\varepsilon}_{\mathrm{eq}}^{\mathrm{cr}} = A \sinh \frac{\sigma_{\mathrm{eq}}}{\sigma_0} \tag{2}$$

- Johnson et al. (1963)

$$\dot{\varepsilon}_{\mathrm{eq}}^{\mathrm{cr}} = A_1 \sigma_{\mathrm{eq}}^{\mathrm{n}_1} + A_2 \sigma_{\mathrm{eq}}^{\mathrm{n}_2} \tag{3}$$

where $\dot{\varepsilon}_{\mathrm{eq}}^{\mathrm{cr}}$ is the equivalent creep strain rate, σ_{eq} is the equivalent stress. a, A, A_1, A_2, σ_0, n, n_1 and n_2 are material parameters.

The results of fitting presented in Figure 8 indicate that the hyperbolic sine function (2) provides the best description of experimental data if compared to the functions (1) and (3). Equation (2) was also applied in Kowalewski et al. (1994) to describe secondary creep for a cast aluminum alloy. To characterize the primary creep stage as well as the strain ratcheting behavior under the reversed or cyclic loading, the back stress tensor $\boldsymbol{\alpha}$ can be introduced. The tertiary creep stage and the softening of stress-strain plots under cyclic stressing can be modeled with the help of a scalar damage variable.

In Kowalewski et al. (1994) it is noted that a single damage variable is not enough for the creep modeling of heat-treatable aluminum alloys. To characterize over-aging effects, an additional state variable is proposed.

We start the decomposition of the total strain tensor $\boldsymbol{\varepsilon}$ into elastic $\boldsymbol{\varepsilon}^{\mathrm{el}}$ and inelastic $\boldsymbol{\varepsilon}^{\mathrm{in}}$ parts

$$\boldsymbol{\varepsilon} = \boldsymbol{\varepsilon}^{\mathrm{el}} + \boldsymbol{\varepsilon}^{\mathrm{in}} \tag{4}$$

where the elastic strain tensor is defined by the Hooke law

$$\boldsymbol{\varepsilon}^{\mathrm{el}} = \frac{1+\nu}{E}\boldsymbol{\sigma} + \frac{\nu}{E}(\mathrm{tr}\boldsymbol{\sigma})\boldsymbol{I} \tag{5}$$

E is the Young's modulus, ν is the Poisson's ratio, $\boldsymbol{\sigma}$ is the Cauchy stress tensor and $\boldsymbol{I}$ is the second rank unit tensor. The constitutive equation for the inelastic strain rate tensor can be formulated as follows

$$\dot{\boldsymbol{\varepsilon}}^{\mathrm{in}} = \frac{3}{2}A\sinh\left\{\frac{\sigma_{\mathrm{eq}}}{\sigma_0(1-\omega)(1-\phi)}\right\}\frac{\boldsymbol{s}-\boldsymbol{\beta}}{\sigma_{\mathrm{eq}}} \tag{6}$$

$$\boldsymbol{s} = \boldsymbol{\sigma} - \frac{1}{3}\mathrm{tr}\boldsymbol{\sigma}\boldsymbol{I}, \quad \boldsymbol{\beta} = \boldsymbol{\alpha} - \frac{1}{3}\mathrm{tr}\boldsymbol{\alpha}\boldsymbol{I} \tag{7}$$

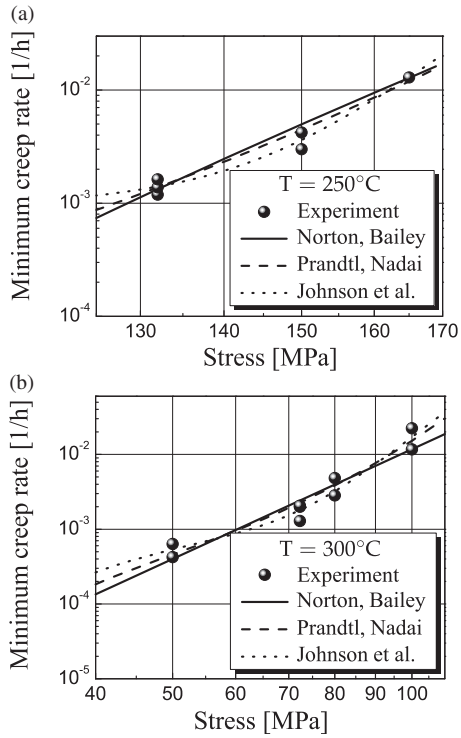

Figure 8. Approximation of minimum creep strain rate at: (a) 250°C and (b) 300°C.

$$\dot{\boldsymbol{\beta}} = A_{\mathrm{h}}\left(\frac{2}{3}\dot{\boldsymbol{\varepsilon}}^{\mathrm{in}} - \dot{\varepsilon}_{\mathrm{eq}}\frac{\boldsymbol{\beta}}{\beta_*}\right), \quad \dot{\varepsilon}_{\mathrm{eq}} = \sqrt{\frac{2}{3}\mathrm{tr}(\dot{\boldsymbol{\varepsilon}}^{\mathrm{in}})^2}, \quad \sigma_{\mathrm{eq}} = \sqrt{\frac{3}{2}\mathrm{tr}(\boldsymbol{s}-\boldsymbol{\beta})^2} \tag{8}$$

In equations (6) to (8) $\boldsymbol{\beta}$ is the deviatoric part of the back stress tensor $\boldsymbol{\alpha}$, $\boldsymbol{s}$ is the deviatoric part of the stress tensor $\boldsymbol{\sigma}$, $\dot{\boldsymbol{\varepsilon}}^{\mathrm{in}}$ is the inelastic strain rate tensor, A, A_{h}, β_* and σ_0 are parameters, $\dot{\varepsilon}_{\mathrm{eq}}$ and σ_{eq} are the equivalent strain rate and the equivalent stress, respectively. To take into account over-aging processes such as coarsening of the strengthening phases Mg_2 Si, for instance, the state variable ϕ is introduced in equation (9). The corresponding evolution equation is postulated here as follows

$$\dot{\phi} = K_{\mathrm{c}}(C_{\mathrm{sat}} - \phi) \tag{9}$$

where K_{c} and C_{sat} are material parameters. The choice of evolution law for ϕ is based on the experimental relationships between the time and the basic mechanical properties of the alloy exposed at different temperatures.

The dominant damage mechanisms include the cracking of particles as well as nucleation of voids and dimples in the matrix around the brittle particles. To characterize these processes in the sense of continuum damage mechanics (Lemaitre and Desmorat, 2005) a scalar damage variable ω is introduced. The corresponding evolution equation is assumed as follows

$$\dot{\omega} = g(\omega)h(\boldsymbol{\sigma})\frac{\dot{\varepsilon}_{\mathrm{eq}}}{\varepsilon_*(\boldsymbol{\sigma})} \tag{10}$$

Table 3. Values of the constitutive model parameters for strain rate, back stress and the aging law.

Temperature (°C)	A (h^{-1})	σ_0 (MPa)	B (MPa)	α_{sat} (MPa)	C_{sat} (h^{-1})	K_{c} –
250	4.88723×10^{-7}	11.6	109000	39	0.0912	0.668
300	1.06842×10^{-4}	12.6	47000	30	0.1443	0.7219

Table 4. Values of the constitutive model parameters for the three damage evolution laws.

		Evolution law		
Temperature (°C)	Parameter	Eqs. (11), (14)	Eqs. (11), (15)	Eqs. (12), (14)
250	k (–)	3.28468	2.32944	5.65694
	a_1 (MPa^{-1})	-1.32846×10^{-4}	–	-5.55475×10^{-4}
	a_2 (–)	0.0905838	–	0.111606
	a_3 (MPa^k)	–	7.716×10^3	–
300	k (–)	2.09247	2.11484	1.69101
	a_1 (MPa^{-1})	-5.88808×10^{-4}	–	-9.05×10^{-4}
	a_2 (–)	0.0910705	–	0.13146
	a_3 (MPa^k)	–	439.846	–

where $g(\omega)$, $h(\boldsymbol{\sigma})$ and $\varepsilon_*(\boldsymbol{\sigma})$ are response functions. Examples for the response functions $g(\omega)$ are

- El Magd and Shaker (1991)

$$g(\omega) = \frac{1}{(1+k)(1-\omega)^k} \tag{11}$$

- Naumenko et al. (2011)

$$g(\omega) = k\omega^{\frac{k-1}{k}} \tag{12}$$

where k is a parameter. The frequently used response function $h(\boldsymbol{\sigma})$ can be written as follows Naumenko et al. (2011)

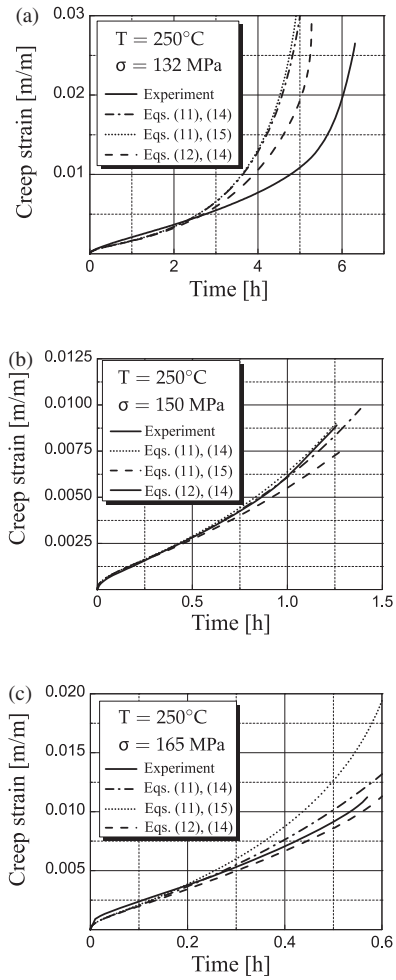

Figure 9. Averaged and predicted creep curves at 250°C under applied maximum stress of: (a) 132 MPa, (b) 150 MPa, and (c) 165 MPa.

$$h(\boldsymbol{\sigma}) = \frac{\sigma_{\mathrm{I}} + |\sigma_{\mathrm{I}}|}{2\sigma_{\mathrm{vM}}}, \quad \sigma_{\mathrm{vM}} = \sqrt{\frac{3}{2}\mathrm{tr}(\boldsymbol{s})^2} \tag{13}$$

where σ_{I} is the first principal stress and σ_{vM} is the von Mises equivalent stress.

The response function $\varepsilon_*(\boldsymbol{\sigma})$ describes the dependence of the creep rupture strain on stress. Below we use the following functions

$$\varepsilon_*(\boldsymbol{\sigma}) = a_1\sigma_{\mathrm{vM}} + a_2 \tag{14}$$

$$\varepsilon_*(\boldsymbol{\sigma}) = a_3\sigma_{\mathrm{vM}}^{-\mathrm{k}} \tag{15}$$

where a_1, a_2 and k are material parameters.

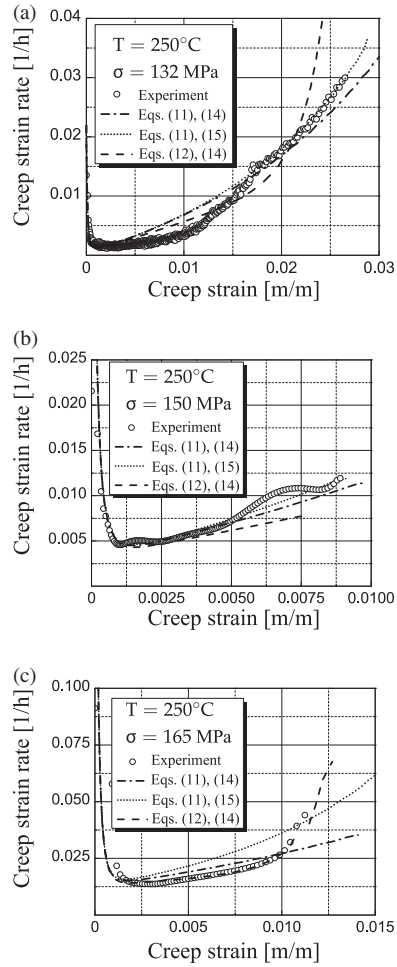

Figure 10. Averaged experimental and predicted creep strain rate vs creep strain curves at 250°C of: (a) 132 MPa, (b) 150 MPa, and (c) 165 MPa.

For the uni-axial stress state equation (6) to (15) of the proposed model can be rewritten as follows

$$\dot{\varepsilon}^{\text{in}} = A \ \sinh\left\{\frac{|\sigma-\alpha|}{\sigma_0(1-\omega)(1-\phi)}\right\}\text{sgn}(\sigma-\alpha) \tag{16}$$

$$\dot{\alpha} = A_{\text{h}}\left(\dot{\varepsilon}^{\text{in}} - \frac{\alpha}{\alpha_{\text{sat}}}|\dot{\varepsilon}^{\text{in}}|\right), \quad h(\sigma) = \frac{\sigma+|\sigma|}{2\sigma}, \tag{17}$$

$$\varepsilon_*(\sigma) = a_1|\sigma| + a_2, \quad \varepsilon_*(\sigma) = a_3|\sigma|^{-\text{k}} \tag{18}$$

Twelve material parameters are calibrated against tensile and creep curves. The values are listed in Tables 3 and 4.

The results of creep tests at 250°C and 300°C are described with the model using three different damage laws. As a representative result, Figures 9 and 11 illustrate the comparison between the averaged experimental creep curves and the model predictions. Additionally, creep strain rate versus creep strain are presented in Figures 10 and 12. One can see that the damage evolution law (10) and response functions (11), (12) and (14) are suitable to fit experimental data.

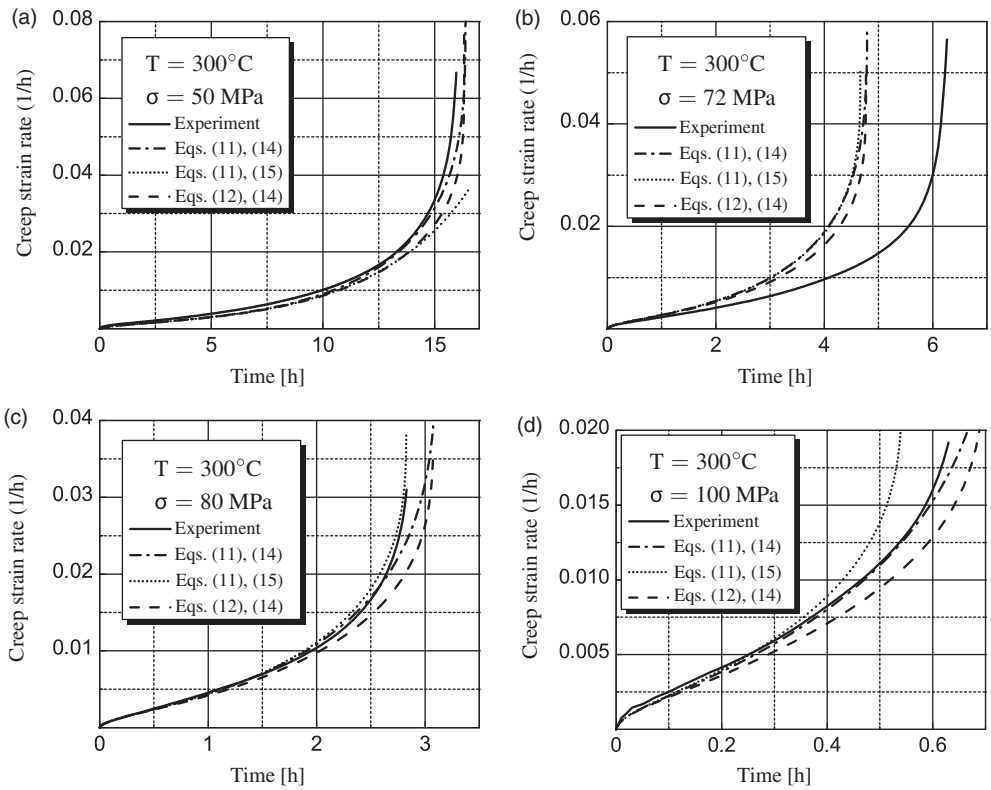

Figure 11. Averaged and predicted creep curves at 300°C under applied maximum stress of: (a) 50 MPa, (b) 72.3 MPa, (c) 80 MPa, and (d) 100 MPa.

The verification of the constitutive model is provided by numerical simulations of force-controlled low cycle fatigue tests at temperatures of 250°C and 300°C. The value of minimum ratcheting strain rate computed by the model and the values determined from the experimental data are plotted in Figure 13 as functions of the maximum stress in a loading cycle. Due to the large scatter of

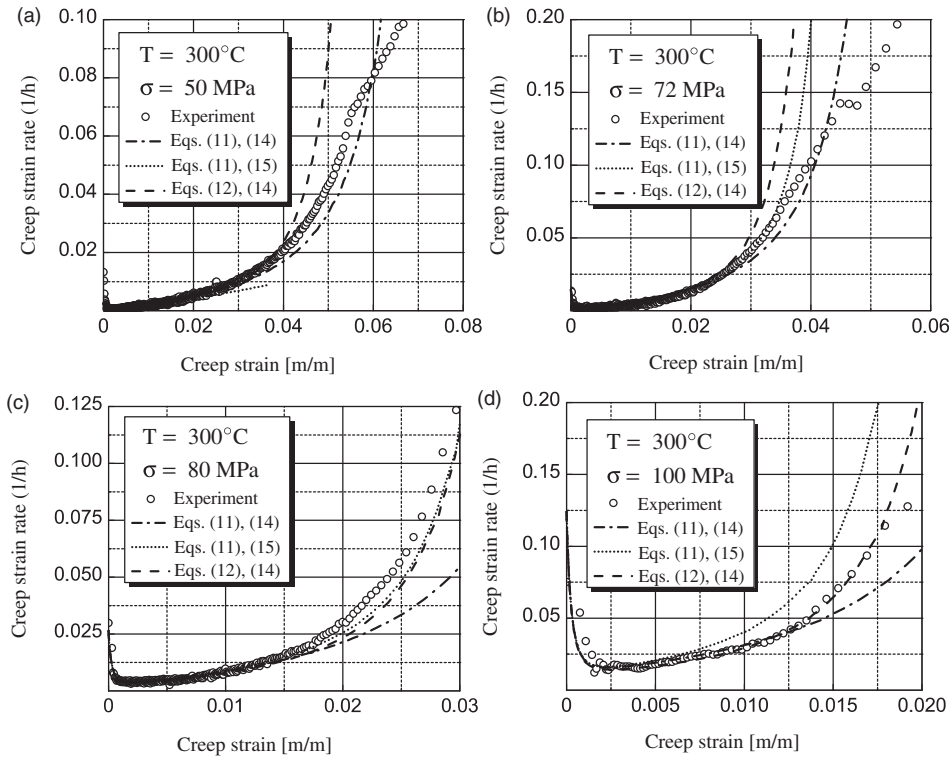

Figure 12. Averaged experimental and predicted creep strain rate vs creep strain curves at 300°C under applied maximum stress of: (a) 50 MPa, (b) 72.3 MPa, (c) 80 MPa, and (d) 100 MPa.

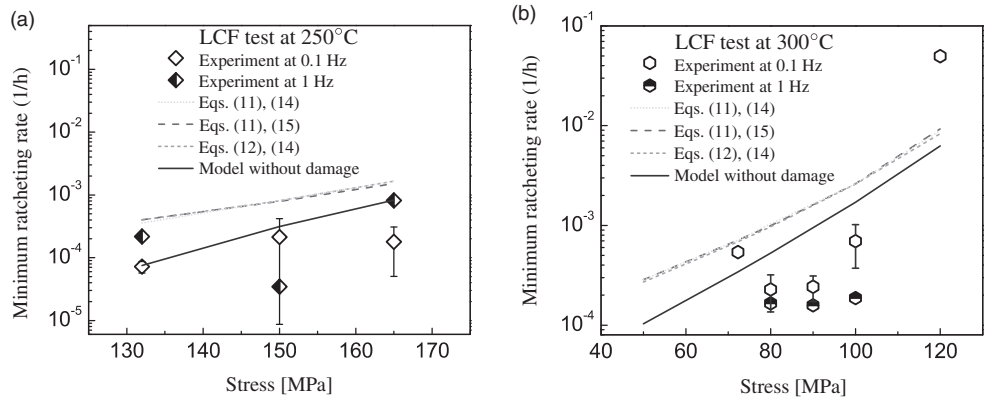

Figure 13. Experimental and predicted minimum ratcheting strain rate vs maximum stress at: (a) 250°C and (b) 300°C.

experimental strain versus time data in cyclic test it was difficult to generate the accurate values of the minimum ratcheting rate. The corresponding scatter bands are given in Figure 13. The predicted values of minimum ratcheting rates are almost insensitive to the loading frequency in the range 0.1–1 Hz. As it can be seen in Figure 13(a), for the temperature level of 250°C the minimum ratcheting rate values are slightly overestimated by the model. The values predicted by the model without damage lie within the scatter bands at 250°C. For the temperature level of 300°C, the model overestimates the values of minimum ratcheting rate even when the damage evolution is disregarded. Based on Figure 14 we conclude that the model can well predict the number of cycles to failure at temperature of 250°C for both loading frequencies. The simulated number of cycles to failure at 300°C and 0.1 Hz, Figure 15(a), are in agreement with the experimental results.

The model predicts too conservative values of the alloy durability for the test data corresponding to the loading frequency of 1 Hz and temperature of 300°C (Figure 15(b)).

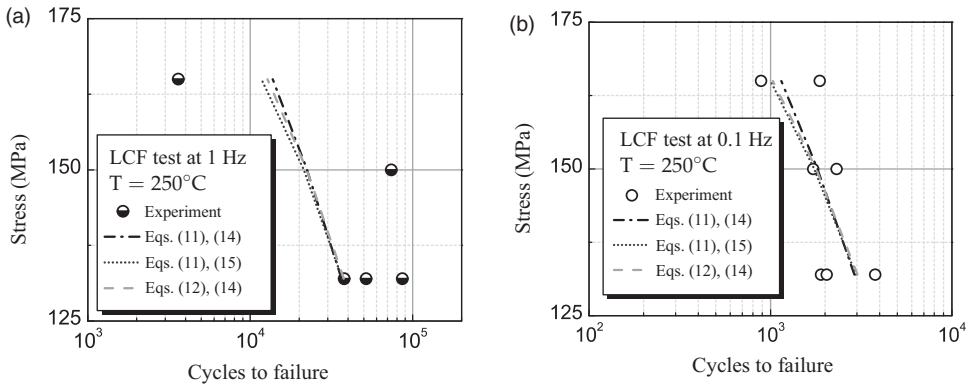

Figure 14. Experimental and predicted fatigue lives in relation with maximum stress at 250°C under load frequency of: (a) 1 Hz and (b) 0.1 Hz.

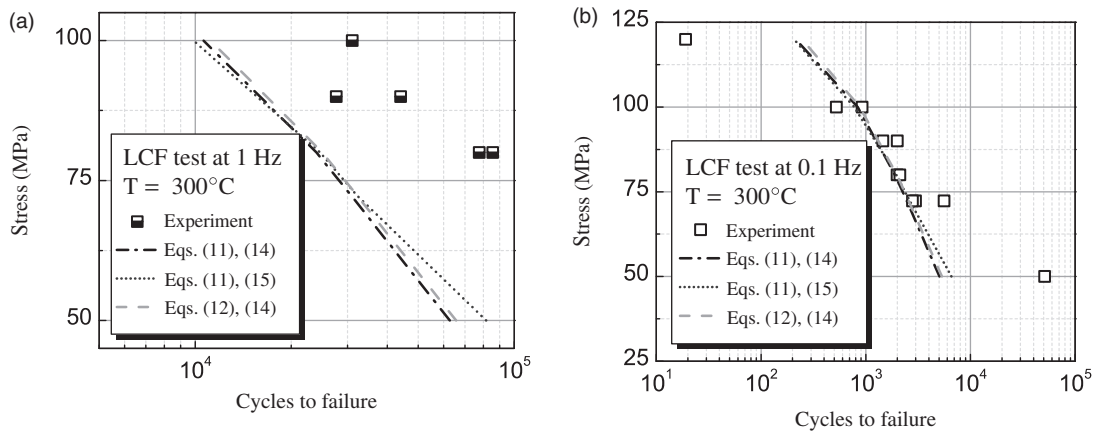

Figure 15. Experimental and predicted fatigue lives in relation with maximum stress at 300°C under load frequency of: (a) 1 Hz and (b) 0.1 Hz.

Conclusions

In this article, a rate-dependent constitutive model was applied to represent the creep test and inelastic deformation in force-controlled low cycle fatigue tests at temperatures of 250°C and 300°C. Based on experimental data from tensile and creep tests, material parameters were identified. The model is applied to predict the ratcheting deformation under cyclic stress test. The computed values of minimum ratcheting strain rates are overestimated in comparison with the experimental data at 300°C. For the temperature level of 250°C the results are in satisfactory agreement with experimental data. Further comparison of the model predictions with test data shows that the fatigue lives are well estimated. An exception is the test at 300°C under loading frequency of 1 Hz, where the model gives conservative number of cycles to failure.

The current experimental data for this alloy is limited to the two temperature levels. Therefore, the sets of material constants were identified independently for these temperature levels. To extend the model for thermo-mechanical fatigue analysis Arrhenius type functions of temperature should be identified in the future.

The parameters in the multi-axial constitutive and evolution equations (6) to (14) were identified from uni-axial tests. The open question is about the accuracy of the assumed equivalent stress expressions. For example, equations (9) and (13) are found to predict tertiary creep of several materials under multi-axial stress state with a good accuracy Naumenko and Altenbach (2007); Naumenko et al. (2011). For the alloy studied in this article experimental data under multi-axial stress state, e.g. tests on notched bars is currently not available. Further verification of the model for the multi-axial stress state should be performed in the future.

As our results show, the damage evolution equation (9) describes well the tertiary creep stage of the considered alloy. However, for cyclic loading conditions equation (9) overestimates ratcheting strains. Indeed, high strain rates during cycles will lead to high damage rates according to equation (9). To remove this spurious damage accumulation, modified dependencies of the damage rate on the stress and the strain rate should be elaborated in the future.

Funding

The authors were supported by the DFG (PhD-School ''Micro-Macro-Interactions in structured Media and Particle Systems'' GRK 828).

References

Abdel Karim M and Ohno N (2000) Kinematic hardening model suitable for ratchetting with steady-state. *International Journal of Plasticity* 16: 225–240.

Ammar H, Samuel A and Samuel F (2008a) Effect of casting imperfections on the fatigue life of 319-F and A356-T6 casting alloys. *Materials Science and Engineering A* 473: 65–75.

Ammar H, Samuel A and Samuel F (2008b) Effect of surface porosity on the fatigue life of AE425 and PM390 hypereutectic Al–Si casting alloys at medium and elevated temperatures. *Materials Science and Engineering A* 473: 58–64.

Chaboche J (2008) A review of some plasticity and viscoplasticity constitutive theories. *International Journal of Plasticity* 24: 1642–1693.

Colak O and Krempl E (2003) Modeling of uniaxial and biaxial ratcheting behavior of 1026 carbon steel using the simplified viscoplasticity theory based on overstress (VBO). *Acta Mechanica* 160: 27–44.

Couper M, Neeson A and Griffiths J (1990) Casting defects and the fatigue life of an aluminum casting alloy. *Fatigue & Fracture of Engineering Materials & Structures* 13: 213–227.

El Magd E and Shaker C (1991) Ein strukturmechanisches Modell für das Kriecverhalten metallischer Werkstoffe bei zeitverändlicher Spannung. *Materialwissenschaft und Werkstofftechnik* 22: 55–62.

Eswara-Prasad N, Vogt D, Bildingmaier T, et al. (2000) Effect of prior fatigue exposure on the creep behaviour of an aluminium alloy (Al-12Si-CuMgNi). *Zeitschrift für Metallkunde* 91: 190–195.

Inoue T, Ohno N, Suzuki A, et al. (1989) Evaluation of inelastic constitutive models under plasticity-creep interaction for 2Cr-1Mo steel at 600C. *Nuclear Engineering and Design* 114: 295–309.

Kang G, Li Y, Gao Q, et al. (2006) Uniaxial ratchetting in steels with different cyclic softening/hardening behaviours. *Fatigue and Fracture of Engineering Materials and Structures* 29: 93–103.

Glatt W and Konzelmann W (eds) (1988) Aluminium-Gußlegierungen: Sekundär-Aluminium; Qualität und Recycling (5. Auflage). Düsseldorf: Giesserei-Verl.

Kowalewski Z, Hayhurst D and Dyson B (1994) Mechanism-based creep constitutive equations for an aluminium alloy. *Journal of Strain Analysis* 29: 309–316.

Krempl E and Choi S (1992) Viscoplasticity theory based on overstress: the modeling of ratchetting and cyclic hardening of AISI type 304 stainless steel. *Nuclear Engineering and Design* 133: 401–410.

Lemaitre J and Desmorat R (2005) *Engineering DamageMechanics*. Berlin-Heidelberg: Springer-Verlag.

Moreira M and Fuoco R (2006) Characteristics of fatigue fractures in Al–Si cast components. *AFS Transactions* Paper 06 122: 1–15.

Naumenko K and Altenbach H (2007) *Modeling of Creep for Structural Analysis*. Berlin-Heidelberg-New York: Springer.

Naumenko K, Altenbach H and Kutschke A (2011) A combined model for hardening,softening, and damage processes in advanced heat resistance steels at elevated temperature. *International Journal of Damage Mechanics* 200: 578–597.

Naumenko K, Kutschke A, Kostenko Y, et al. (2011) Multi-axial thermomechanical analysis of power plant components from 9-12% Cr steels at high temperature. *Engineering Fracture Mechanics* 78(8): 1657–1668.

Ohno N and Wang J (1995) On modelling of kinematic hardening for ratcheting behaviour. *Nuclear Engineering and Design* 153: 205–212.

Silva F (2006) Fatigue on engine pistons: a compendium of case studies. *Engineering Failure Analysis* 13: 480–492.

Stroppe H (2000) Einfluß der Porosität auf die mechanische Eigenschaften von Gußlegierungen. *Giessereiforschung* 252: 58–60.

Yang X (2007) A unified time dependent model for low cycle fatigue and ratchetting failure based on micro-crack growth. *Nuclear Engineering and Design* 237: 1381–1387.

Yang X, Chow C and Lau K (2003) A unified viscoplastic fatigue damage model for 63Sn- 37Pb solder alloy under cycilc stress control. *International Journal of Damage Mechanics* 12: 225–243.

Ye H (2002) An overview of the development of Al–Si-alloy based material for engine applications. *Journal of Materials Engineering and Performance* 12: 288–297.

Zhan Z-L and Tong J (2007) A study of cyclic plasticity and viscoplasticity in a new nickelbased superalloy using unified constitutive equations. *Part I: Evaluation and determination of material parameters, Mechanics of Materials* 39: 64–72.